The impact of crustal scattering on body-wave reflection interferometry by cross-correlation and multidimensional deconvolution

Hartstra, Iris; Wapenaar, Kees

DOI
10.1093/gji/ggad342

Publication date
2023

Document Version
Final published version

Published in
Geophysical Journal International

Geophysical Journal International

Geophys. J. Int. (2023) **235,** 1996–2006
Advance Access publication 2023 September 02
GJI Seismology

https://doi.org/10.1093/gji/ggad342

The impact of crustal scattering on body-wave reflection interferometry by cross-correlation and multidimensional deconvolution

Iris Hartstra [1,2] and Kees Wapenaar [2]

[1] *Department of Resilient Ports and Coasts, Deltares, P.O. Box* 177, 2600 *MH Delft, The Netherlands. E-mail: iris.hartstra@deltares.nl*
[2] *Department of Geoscience and Engineering, Delft University of Technology, P.O. Box* 5048, 2600 *GA Delft, The Netherlands*

Accepted 2023 August 30. Received 2023 August 25; in original form 2022 December 21

SUMMARY

Previous studies indicate that scattering may pose a trade-off for the performance of seismic interferometry (SI) applications for retrieving body-wave reflections of a target reflector. While it has been demonstrated that a higher scattering strength of the overburden improves the Green's function estimated by cross-correlation SI, other theoretical and empirical studies showed that multiple scattering also gives rise to more artefacts. The implications of this trade-off are analysed in this numerical study for a lithospheric scenario with varying crustal scattering strength and passive illumination conditions. In this scenario, we apply SI by cross-correlation to elastodynamic responses to double-couple sources to reconstruct virtual Moho primary reflections. We include multidimensional deconvolution (MDD) methods in the analysis to investigate whether scattering-induced artefacts affect MDD methods in a similar way as was shown for the cross-correlation method. Our results show that there indeed exists a trade-off between the quality of the virtual primary reflection of the target that can be obtained by SI and the scattering strength of the overburden. Furthermore, we find that the full-field MDD method proves to be most resilient to the negative effects of multiple scattering for all illumination conditions and scattering strengths analysed.

Key words: Inverse theory; Numerical modelling; Body waves; Coda waves; Seismic interferometry; Wave scattering and diffraction.

1 INTRODUCTION

Natural earthquake hypocentres generally concentrate around active plate boundaries such as subduction zones and orogenies. The resulting sparse distribution of earthquakes poses a challenge for seismic interferometry (SI) to estimate virtual body-wave reflections. When the seismic array is not located within the area of the epicentre, the recordings may be insufficiently dominated by events that are within the Fresnel zone with respect to the array. These stationary-phase events are required to obtain a reliable Green's function estimate (Snieder 2004) and a lack thereof likely results in severe contamination by artefacts. Since it is difficult to know whether the features retrieved correspond to artefacts or not, it is important to ensure that an interferometry experiment is conducted under the best possible circumstances.

Various SI studies have shown that multiple scattering can positively influence the estimation of the Green's function by cross-correlation (Derode *et al.* 2003; van Tiggelen 2003; Malcolm *et al.* 2004). Even under limited illumination conditions, sufficiently long recordings of scattering coda can provide the required stationary-phase events (Campillo & Paul 2003; Larose *et al.* 2004; Campillo 2006). However, Snieder & Fleury (2010) and Halliday & Curtis (2009) demonstrate theoretically that multiple scattering increases the number of artefacts in the cross-correlation results considerably. In fact, they show that cancellation of these spurious events relies on sufficient direct wave illumination by passive sources from all angles, which would imply that, in the case of incomplete illumination, a high scattering strength decreases the quality of the full Green's function retrieval. These findings are corroborated by Larose *et al.* (2008), who demonstrate that spurious events in the Green's function estimate decrease with increasing number of sources. Moreover, multiple scattering in the overburden diminishes the visibility of the target reflector, which poses a challenge for both passive and active seismic configurations.

For the performance of multidimensional deconvolution (MDD) methods, multiple scattering may pose a disadvantage as well, but for a different reason. Besides a densely sampled receiver array, MDD methods rely on an acceptable estimation of each earthquake

recording without the free-surface multiples: the V^o field (Wapenaar *et al.* 2008; Hartstra *et al.* 2017; Almagro Vidal 2017; Boiero *et al.* 2023). When the medium is not known, the only plausible estimation of this field can be made by approximating it by the direct arrival of the passive recording, since removing free-surface related multiples from passive data is very challenging. This approximation is acceptable in case the medium has a relatively low scattering strength, because the difference between the full passive recording and the V^o field will be minimal. However, with increasing scattering strength, more energy from the direct arrivals will partition into the scattering coda (Sato *et al.* 2012), which consists of a complex mix of scattered arrivals that did or did not interact with the free surface. Therefore, an increase in scattering strength of the overburden will likely cause the direct-wave approximation of the V^o to become less reliable, which is expected to have a negative impact on the stability of the inversion that underlies MDD (van der Neut & Herrmann 2013).

These considerations imply that scattering poses a trade-off for the performance of SI applications. Considering that the crustal lithosphere has a scattering strength that strongly varies as a function of frequency and area, that is especially high in tectonically active areas (Sato *et al.* 2012), this trade-off is non-trivial for applications of seismic body-wave interferometry to real data (Roux *et al.* 2005; Ruigrok *et al.* 2011; Nakata *et al.* 2014; Almagro Vidal *et al.* 2018; Chamarczuk *et al.* 2021). In the current work, we conduct a 2-D numerical study to assess the impact of increasing scattering strength of the crustal overburden on the ability of correlation- and deconvolution-type SI methods to estimate the target body-wave reflection under different illumination conditions. This way, we aim to determine which of the SI methods for body-wave reflection estimation is most stable for use in real-world settings characterized by multiple scattering. We base the design of our numerical models on a lithospheric model that is characterized by a heterogeneous crustal overburden overlying a homogeneous mantle (Margerin *et al.* 1998, 1999; Heller *et al.* 2022). We neglect anelastic effects, because it has been shown that for low frequencies (∼1 Hz) intrinsic absorption has a negligible effect on the coda decay compared to the lithospheric leakage effect (Margerin *et al.* 1999). Finally, we estimate the scattering coda quality factor to verify that the scattering regime we analyse is dominated by multiple scattering (Aki 1969; Wu & Aki 1985) by using the observed trend between the coda quality factor and the mean free path length for different crustal thicknesses (Margerin *et al.* 1999).

1.1 Outline

In Section 2, we conduct a numerical study in order to investigate the relation between multiple scattering in the overburden and the quality of the primary-reflection estimation with correlation- and deconvolution-type SI methods. Section 2.1 describes the three models of the lithosphere with varying scattering strength that we use to simulate the elastodynamic particle-velocity responses to passive double-couple sources. Here, we perform a scattering analysis by estimating the coda quality factor for the two models that have a heterogeneous crust. From these simulated passive recordings, we estimate the virtual primary reflections of the Moho reflector in each of the three models using the SI methods described in Section 2.2. For each lithospheric model, the SI results are compared to the corresponding reference response in Section 2.3. The numerical study is followed in Section 3 by a discussion of the implications of our results for using SI methods in heterogeneous lithospheric settings and a conclusion in Section 4.

2 NUMERICAL STUDY

The numerical simulations are conducted using the elastic finite-difference scheme of the 2-D seismic propagation model `fdelmodc` (Thorbecke & Draganov 2011) in order to take into account *P* waves and vertically polarized *S* waves. This scheme also models the *SV*-to-*P* and *P*-to-*SV* converted waves (abbreviated to *SP*-converted waves in this study), which play a dominant role in the multiple scattering regime (Weaver 1982; Aki 1992; Snieder 2002). Furthermore, modelling with an elastic scheme allows for the implementation of sources that generate both *P*- and *S*-wave polarizations with the double-couple source type that represents the radiation of fault-slip movement (see fig. 2 in Hartstra *et al.* 2018). All passive-source functions are modelled with a Ricker wavelet with a peak frequency of 1.1 Hz that varies in amplitude among sources. The horizontal and vertical particle velocities are recorded at the surface by 200 receivers with an inter-receiver spacing of 1 km.

2.1 Description of the lithospheric models

To create the synthetic data sets of passive recordings, we use a simplified model of the lithospheric crust, whereby the crust represents the overburden and the Mohorovičić transition (Moho) the target reflector (Mohorovičić 1910; Mooney & Meissner 1992). The 2-D models are bounded by an absorbing boundary to avoid spurious model reflections, with the exception of the acquisition surface: here a free surface boundary condition is implemented, which ensures Rayleigh waves and free-surface multiples to be present in the modelled passive data. For the lithospheric background velocities, we choose values that are roughly based on the PREM model (Dziewonski & Anderson 1981). The crust has background *P*- and *S*-wave velocities of 6 and 3.5 km s^{-1}, respectively, and a density of 2700 kg m^{-3}. The denser mantle material has *P*- and *S*-wave velocities of 9 and 4.5 km s^{-1}, respectively, and a density of 3400 kg m^{-3}. The Moho transition between crust and mantle is modelled as a horizontal reflector at 50 km depth, which is close to the average Moho depth typically estimated for continental collision zones (Stein & Wysession 2003). Different numbers of crustal scatterers with a diameter of 2 km are introduced in the crustal overburden to create models with various scattering strengths. The scatterers have a lower *P*- and *S*-wave velocity and density than the crust: 5.5 and 3.3 km s^{-1} and 1500 kg m^{-3}, in that order. These scatterers are expected to generate a wavefield dominated by Mie scattering, because their size is of the same order as the dominant *S* and *P* wavelengths in the crust (for 1.1 Hz): 3.2 and 5.5 km, respectively (Wu & Aki 1985). The first model is defined by a homogeneous lithospheric crust (Fig. 2a), the second contains 50 spherical crustal scatterers with a lower velocity and density as specified above (Fig. 5a) and the final model contains 200 scatterers of the same type (Fig. 6a). Note that by increasing the number of scatterers, the mean free path length decreases.

2.1.1 Analysis of scattering properties

To complete the description of the lithospheric models, we conduct a scattering coda analysis of the models with 50 and 200 scatterers to estimate their scattering properties. Many studies (Aki 1969; Wu &

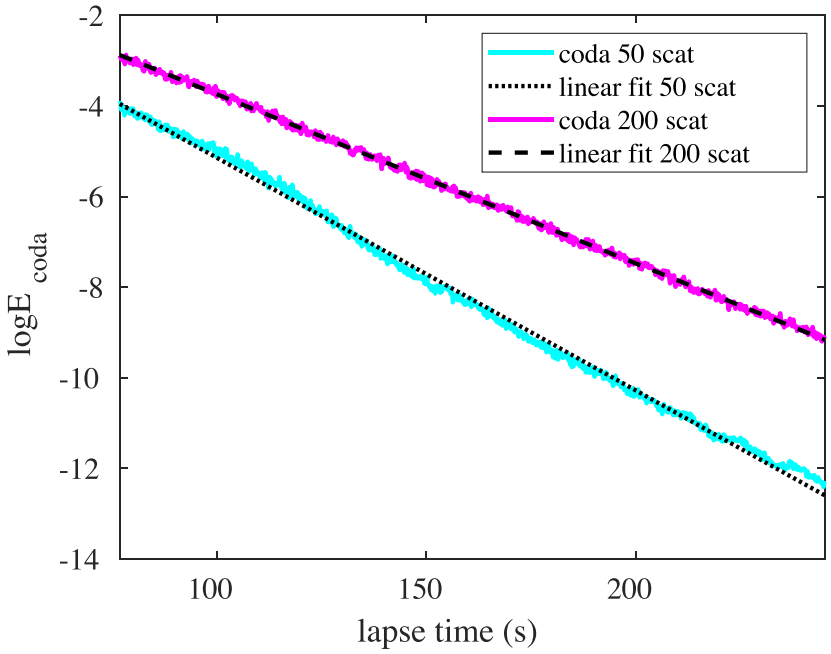

Figure 1. Scattering coda analysis: the cyan and magenta plots indicate the natural logarithm of the averaged energy density for selected passive-source recordings of the models with 50 and 200 scatterers, respectively. The black dotted and dashed lines indicate the obtained fit by linear regression.

Aki 1985; Margerin *et al.* 1999; Sato *et al.* 2012) have demonstrated the practical use of the empirical relation to estimate the coda quality factor Q_C from the energy density decay of scattering coda, E, which we reproduce here using the notation by Wang & Shearer (2019):

$$E(f,t) = S(f)R(f)t^{-\alpha}\exp\left(-\frac{2\pi f t}{Q_C(f)}\right), \quad (1)$$

where $S(f)$ is a frequency-dependent source term, $R(f)$ a frequency-dependent station term, α a dimensionality factor of the spreading term and t is lapse time. Note that eq. (1) represents the diffusion approximation to the radiative transfer equation, which, in the longer lapse time limit or when the mean free path length of the scattering slab is smaller than the crustal thickness, is valid to describe the scattering process (Margerin *et al.* 1998). Moreover, comparisons of eq. (1) to the exact radiative transfer equation in Margerin *et al.* (1999) show that it is acceptable to employ this equation to obtain a reliable estimate of the coda quality factor. To this end, we adopt an approach based on multistation and multievent method (MSMEM) detailed in Wang & Shearer (2019). In short, this approach involves taking the natural logarithm of eq. (1), which yields the following linear equation that serves to estimate the coda quality factor Q_C by linear regression:

$$\log(E(f,t)) = \log(S(f)) + \log(R(f)) - \alpha\log(t) - \frac{2\pi f t}{Q_C(f)}, \quad (2)$$

To this end, first the average energy-density variation as a function of lapse time is calculated for the two models that have a heterogeneous crust (Figs 5a and 6a) by selecting a total of 400 traces of source–receiver pairs that combine 20 regularly spaced receivers and 20 passive sources along the Moho reflector. Note that a single trace suffices for this calculation, but by averaging over a large amount of traces, we can obtain a more robust estimation and a better coverage of the scattering slab. Next, the natural logarithm of the result is corrected to compensate for geometrical spreading by adding the term $\alpha\log(t)$. Note that in equivalent 3-D scenarios describing the longer time limit of body-wave scattering in the crust, geometrical spreading is best approximated by that of 2-D diffusion with a corresponding α value of 1 (Margerin *et al.* 1998). In these scenarios, the crust effectively behaves as a 2-D slab, because its finite thickness becomes negligible with respect to the longer path lengths of the scattered body waves. From this, it follows that the energy transport in the equivalent 2-D scenarios of the current modelling study is best described by a 1-D diffusion process, which requires setting the α value to $\frac{1}{2}$ (Paasschens 1997). As a final step, a linear regression algorithm is employed to estimate the slope (β) of the averaged intensity, which facilitates the estimate of the representative coda quality factor of the upper crust for the centre frequency of 1.1 Hz as follows:

$$Q_C(f) = -\frac{2\pi f}{\beta}. \quad (3)$$

For the model with 50 scatterers, a coda quality factor value of 134 is estimated by the regression analysis (cyan plot in Fig. 1), while for the model with 200 scatterers a Q_C value of 185 is found (magenta plot in Fig. 1). Hence, this follows a trend of a decreasing Q_C for an increasing mean free path length. This trend is characteristic of the diffusion regime, as can be observed in fig. 3 of Margerin *et al.* (1999), which shows the relation between mean free path length and the coda quality factor at 1 Hz for different crustal thicknesses: the Q_C decreases with increasing mean free path length in the diffusion limit (the multiple scattering regime), while an increasing trend characterizes the single scattering regime. This indicates that the scattering coda is dominated by multiple scattering, and thus that the observed energy decay rate is ascribed to the effect of energy leakage into the underlying homogeneous mantle due to scattered waves that impinge the Moho below the critical angle. Finally, we estimate the characteristic residence time, τ_d, of diffusive waves in the crust (Margerin *et al.* 1999) for each of the two models for the dominant frequency f of 1.1 Hz:

$$\tau_d = \frac{Q_C}{2\pi f}, \quad (4)$$

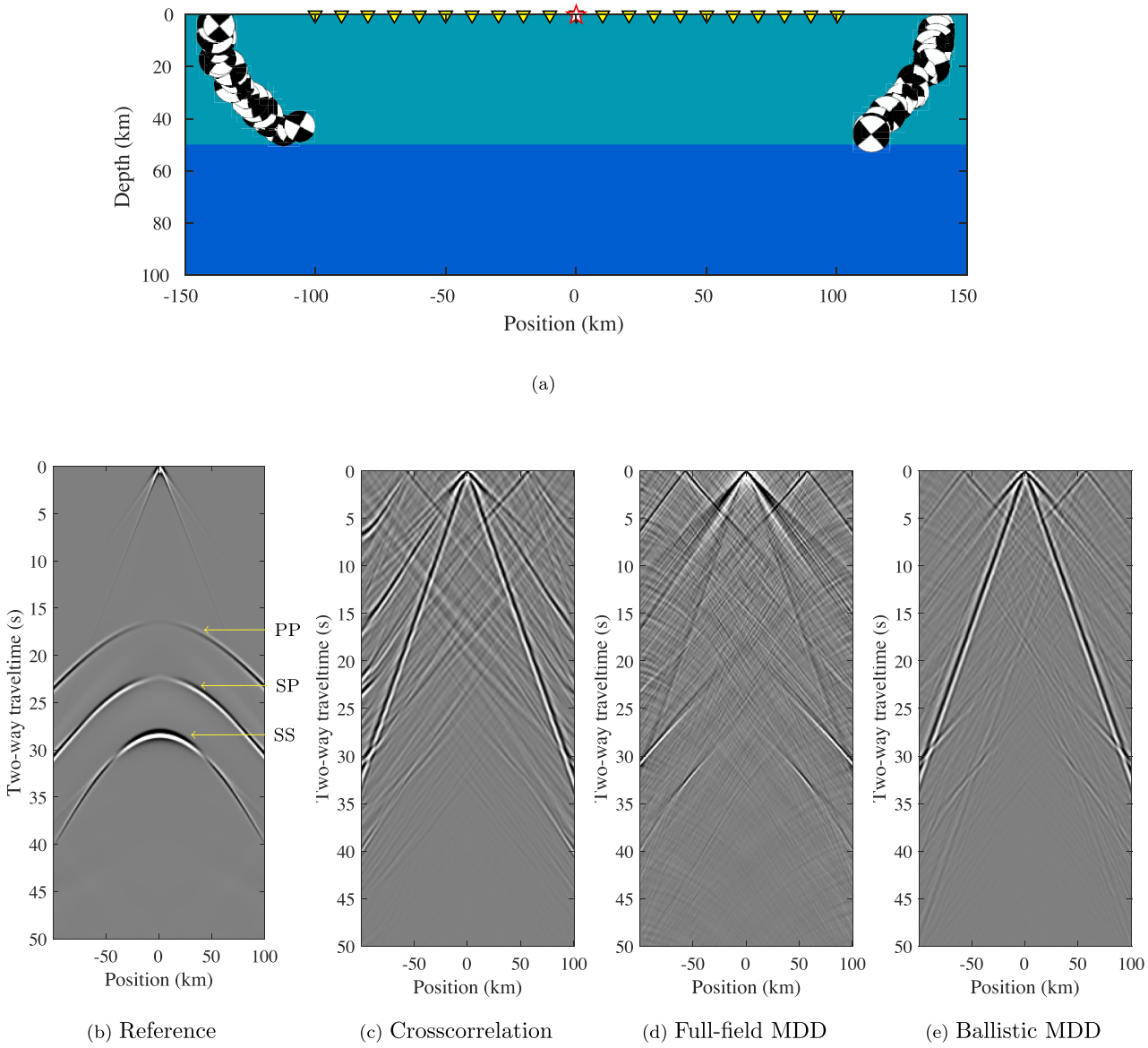

Figure 2. Lithospheric model with a homogeneous crust for limited illumination. (a) Lithospheric model with homogeneous crust. (b) Reference horizontal particle-velocity response to a horizontally oriented double-couple source at the middle receiver position. (c) Horizontal particle-velocity response to a virtual horizontal source estimated with SI by cross-correlation. (d) Same as (c), but with full-field MDD. (e) Same as (c), with ballistic MDD.

which yields a greater residence time for the model with 200 scatterers (29 s) than for the model with 50 scatterers (21 s).

2.1.2 Modelled reference responses

For each of the three models (Figs 2a, 5a and 6a), as a reference response we simulate the horizontal particle-velocity responses to a horizontally oriented double-couple source implemented at the virtual source position, which we choose to place at the central receiver position at the acquisition surface (see red star in Figs 2b, 5b and 6b). Modelled reference responses are required to determine the correct two-way traveltime (TWT) and the relative amplitude variation versus offset (AVO) of the primary reflections, which is necessary information to be able to correctly distinguish virtual primary reflections from artefacts in virtual responses obtained by SI methods. In each reference response, the *PP*- and *SP*-converted, and *SS* primary reflections can be distinguished for increasing TWT (as designated in Figs 2b, 5b and 6b). Due to the horizontal orientation of the double-couple source, both the *PP*- and *SP*-converted primary reflections show a very low amplitude for near-offset while the *SS* primary reflection symmetrically switches polarity around 45 km offset. Further analysis of the reference responses shows that as the scattering strength of the crust increases, the wavefield becomes more complex due to diffractions that thus cause the primary reflections to become more obscured.

2.2 SI methods

The elastodynamic forms of SI by cross-correlation (Wapenaar & Fokkema 2006), ballistic MDD (Wapenaar *et al.* 2008) and full-field MDD (Hartstra *et al.* 2018) are applied to the synthetic data sets to estimate the horizontal particle-velocity responses to a horizontally oriented virtual source located at the middle receiver of the surface array. The mathematical forms and implementation of these

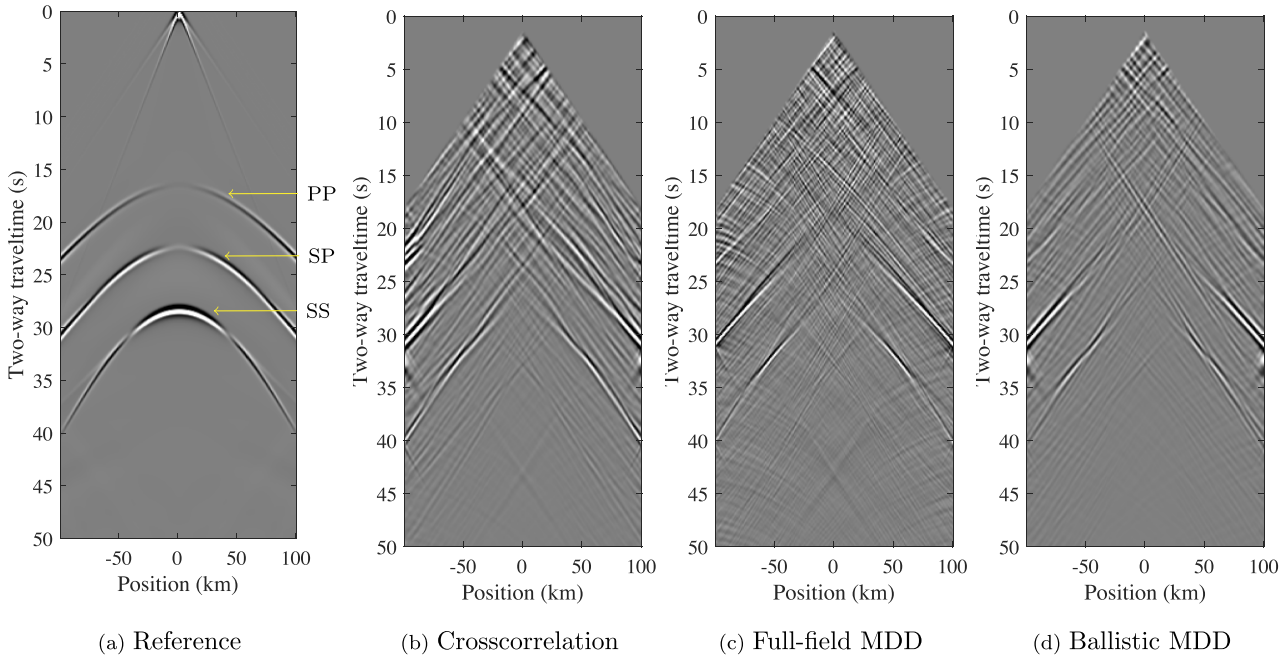

Figure 3. As Fig. 2, but with early arrivals muted and high-wavenumber surface waves and artefacts suppressed.

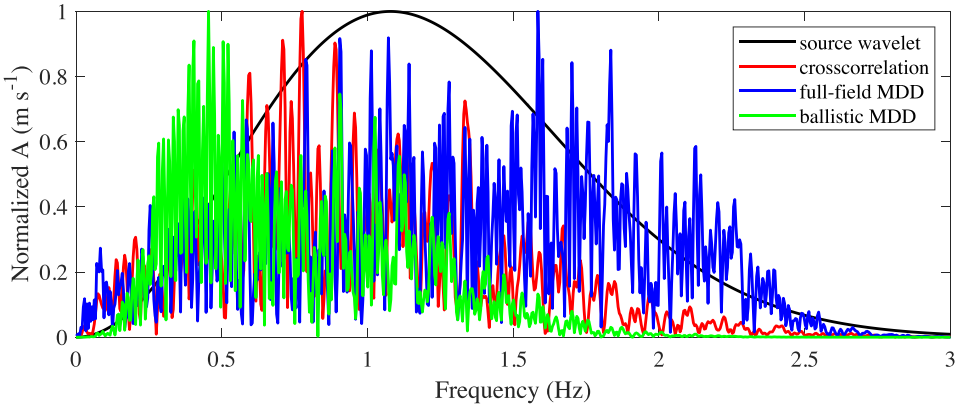

Figure 4. Frequency spectrum analysis of single traces selected from virtual SI responses obtained in the numerical experiment in the model with a homogeneous crust and limited illumination (Fig. 2a).

three SI methods are detailed in eqs (1), (10) and (13) of Hartstra *et al.* (2018), respectively. In this study, we choose to only analyse the horizontal component of the receiver and virtual source of the Green's function estimates, but we emphasize that any other combination of components can be obtained equally well. Note that each of these three SI methods estimates the Green's function response to a different type of virtual-source mechanism. For the full-field MDD method, this is a double-couple point source, whereby in this study the fault slip occurs horizontally along a plane with a vertical normal vector resulting in a point source of simple-shear stress: τ_{13}. Note that this source is defined in a medium without free surface, because full-field MDD estimates the Green's function response of the equivalent medium without free surface. This is in contrast to ballistic MDD, which estimates the Green's function response of the medium with free surface to a point source of horizontally oriented force: f_1. The cross-correlation method estimates the same type of Green's function as ballistic MDD, but for an inherent convolution with the averaged auto-correlation of the passive-source functions.

Given the fact that in the field the source wavelets of the naturally occurring sources cannot be known exactly, in this study we choose to refrain from any wavelet processing. This is expected to cause spectral differences between the results. Note that both MDD methods require time-windowing to either select or (partially) remove the direct arrival: full-field MDD in the correlation function and ballistic MDD in both the correlation function and the point spread function (PSF). We find the best results when setting the length of this time window to five times the peak period, which yields a total length of 4.5 s in this configuration. Following the approach in Almagro Vidal (2017) and Hartstra *et al.* (2018), we apply a taper to the time window to minimize artefacts as much as possible.

2.3 Comparison of SI results

In order to simulate the situation of sparse illumination, the passive sources are restricted to the outer sides of the model as shown

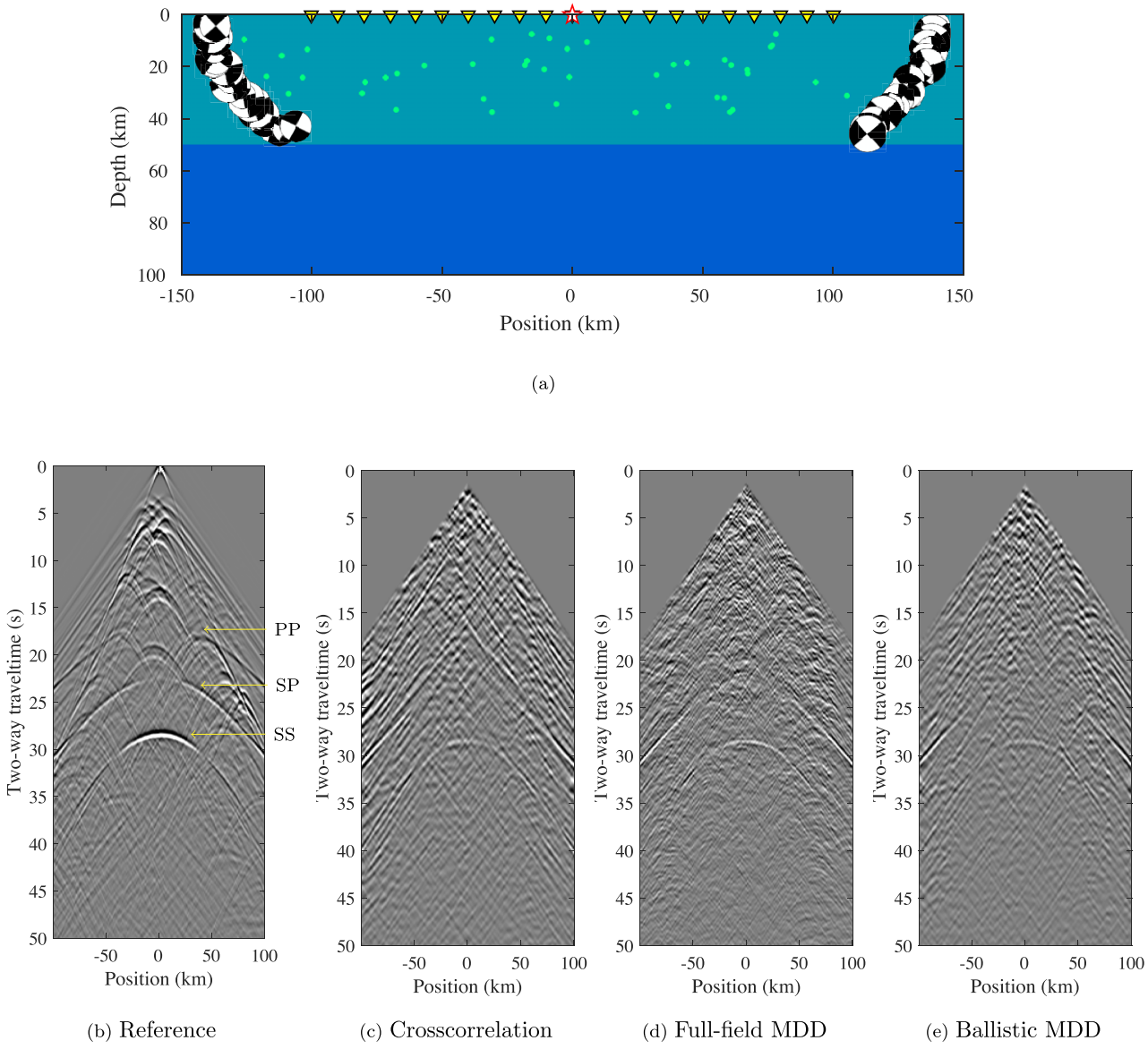

Figure 5. As Fig. 2, but with 50 scatterers in the crust.

in Fig. 2(a). This ensures that the direct incident waves do not provide low wavenumbers (waves coming directly from below) to the virtual source position at the array. This configuration results in passive-source illumination that is limited to surface and body waves for higher wavenumbers, which poses a challenge for the SI methods to estimate the complete wavenumber spectrum of the primary reflections.

2.3.1 Homogeneous crust

In the first experiment, we apply the three SI methods to the synthetic data set obtained for the model with a homogeneous crust (Fig. 2a). The comparison of the SI results in Fig. 2 shows that the body-wave reflections are difficult to discern in the cross-correlation and ballistic MDD result due to the dominant presence of the surface wave. On the other hand, the surface wave in the full-field MMD result is barely visible, but this result reveals the three primary reflections partially for higher offsets (see Fig. 2d). This is in accordance with the governing theory, which dictates that, different from cross-correlation and ballistic MDD, the full-field MDD estimates the Green's function response of the equivalent medium without free surface. Considering that the objective of this study is to analyse the quality of the estimation of the three body-wave primary reflections indicated in Fig. 2(b), we apply further processing to the SI results from here onwards: the early arrivals up to the direct arrival of the *P* wave are muted and an *fk*-filter is applied to remove high-wavenumber events, such as surface waves and steep-dipping artefacts (see Fig. 3). After processing, the cross-correlation result reveals sections of the *SS* primary reflection for offsets larger than about 40 km and the *SP*-converted primary reflection for offsets larger than 70 km, but it is still affected by the presence of artefacts (Fig. 3b). The result of ballistic MDD in Fig. 3(d) shows an improvement with respect to the cross-correlation result, because it is clearly less dominated by artefacts. The *SP*-converted Moho pri-

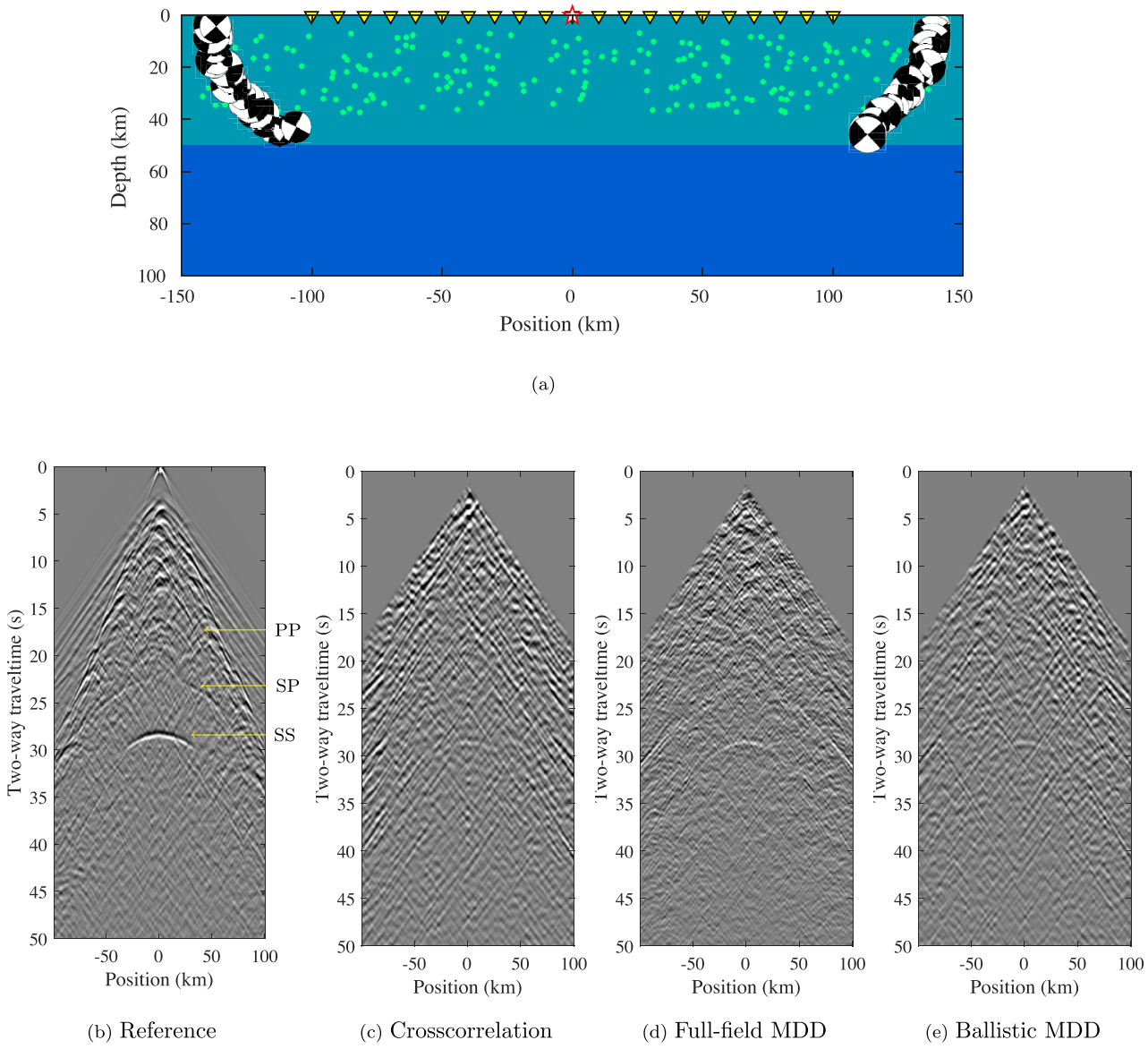

Figure 6. As Fig. 2, but with 200 scatterers in the crust.

mary reflection is obtained for offsets as small as 40 km and the *SS* Moho primary reflection for an even smaller offset of 30 km. However, for smaller offsets these primary reflections follow a straight continuous slope that does not correspond to the TWT values observed in the reference response (Fig. 3a), which shows that this is an artefact. The virtual response estimated by full-field MDD is similar in quality to the ballistic MDD result (Fig. 2d) and does not offer any obvious improvements in this homogeneous crustal model.

Since we do not apply wavelet processing, the spectral content of the three SI results is different. Fig. 4 shows the frequency spectra of the unfiltered results obtained from each of the three SI methods for the configuration in Fig. 2(a), where the amplitudes (A) are normalized with respect to the maximum amplitude of the respective spectra. Note that the spectra of ballistic MDD and cross-correlation are both dominated by lower frequencies, while full-field MDD shows an amplification of the higher frequencies, resulting in a considerably broader frequency spectrum. This difference is partly due to the strong prevalence of low-frequency surface waves in this configuration that is characterized by shallow passive sources (see Fig. 2a). The full-field MDD result is hardly affected by surface waves as this method estimates the Green's function in an equivalent medium without free surface, while cross-correlation and ballistic MDD retrieve the result with free-surface interactions. In this scenario, the spectrum of the ballistic MDD result is most inclined to lower frequencies, which is likely due to the use of the time window when selecting the direct arrivals for constructing the ballistic PSF. Different from ballistic MDD, the PSF of the full-field MDD method contains the entire wavefield and therefore is unaffected by time-windowing.

2.3.2 Heterogeneous crust with 50 scatterers

When 50 circular scatterers are introduced in the lithosphere to effectively increase its scattering strength (Fig. 5a), more waves

with low wavenumbers that are in stationary phase illuminate the Moho and the array. The reference response for this model shows that the scattering almost completely obscures the visibility of the *PP* reflection (Fig. 5b). Therefore, it is no surprise that the three virtual reflection responses do not reveal it either. The full-field MDD result in Fig. 5(d) clearly shows that the *SS* primary reflection is now also visible for very low offsets: even vertical incidence *S*-wave reflections are retrieved. The *SP* Moho reflection is better resolved and less obscured by artefacts than in Fig. 3(c). Although more affected by artefacts than the full-field MDD result, the cross-correlation method also shows the *SS* primary reflection (Fig. 5c). This indicates that cross-correlation can profit from the increased illumination provided by the crustal scattering. Nevertheless, the result is clearly more affected by scattering-induced artefacts than full-field MDD. In the ballistic MDD result in Fig. 5(e), it is easier to discern the *SP*-converted reflection from steep-dipping artefacts than in the cross-correlation result. Moreover, different from the cross-correlation result, both MDD methods show that some diffraction hyperbolae from the crustal scatterers are retrieved as well. Yet, the virtual diffraction hyperbolae are more pronounced and less obscured by artefacts in the full-field MDD result than in the ballistic MDD result.

2.3.3 Heterogeneous crust with 200 scatterers

When the scattering strength is further increased by implementing 200 crustal scatterers (Fig. 6a), the reference response in Fig. 6(b) shows that the increased complexity of the overburden diminishes the visibility of the Moho primary reflections. The cross-correlation and ballistic MDD results still show a trace of the *SS* primary reflection for this increased scattering strength (Figs 6c and e, respectively), but the *SP*-converted reflection is now severely obscured by artefacts. The slightly diminished occurrence of artefacts in the ballistic MDD result indicates that this method still holds an advantage over cross-correlation in this scenario. The full-field MDD result in Fig. 6(d) reveals the *SS*- and *SP*-converted primary reflections, but the visibility is slightly decreased with respect to the scenario with less scatterers in Fig. 5(d). Since this decreased visibility is also observed in the reference response (Fig. 6b), this is not necessarily indicative of a lower performance. Note that diffraction hyperbolae can be discerned in the full-field MDD result: for example, around a TWT of 10 s at an offset of about 5 km and around a TWT of 13 s at 0 offset.

In order to establish the effect of multiple scattering without the negative impact of sparse illumination in this example, a final numerical modelling experiment is conducted for the case of more optimal illumination conditions. A total of 100 passive sources that illuminate the array from all angles are implemented in the model with 200 scatterers (Fig. 7a). For this configuration, the result estimated with cross-correlation shows a clearer *SS* primary reflection (Fig. 7c) than in the case of limited illumination (Fig. 6c). The *SP*-converted primary reflection is now a bit more visible under full illumination conditions. Ballistic MDD offers an improvement with respect to the cross-correlation result by effectively reducing the prevalence of artefacts (Fig. 7e). The full-field MDD result reveals both the *SS*- and *SP*-converted primary reflections, which match the reference response in Fig. 7(b) in terms of TWT and relative variation of AVO. Also note the accurate estimation of the polarity shift along the *SS* primary at an offset of about 45 km. The crustal diffractions are not completely retrieved by full-field MDD, but this has the advantage that full-field MDD now partially reveals the *PP* primary reflection. In fact, the *PP* primary reflection is clearer in the full-field MDD virtual response than in the modelled reference response in Fig. 7(b).

3 DISCUSSION

Our numerical results show that when passive illumination is limited to high wavenumbers, multiple crustal scattering can improve the interferometric retrieval of the target reflection primaries by complementing the limited illumination with lower wavenumbers. However, the results also show that increasing scattering strength does not only benefit the retrieval of primary reflections by SI methods.

3.1 Effects of multiple scattering on SI methods

Increasing the scattering strength of the crustal overburden brings SI by cross-correlation more low-wavenumber reflections to exploit in the case of limited passive-source illumination. However, our observations showed that under limited illumination conditions, increasing the crustal scattering strength also introduces significantly more artefacts (compare Fig. 5c to 6c). The higher complexity of the medium provides more opportunities for artefacts to be created, which cannot be cancelled out when the direct illumination by the passive sources is incomplete (Halliday & Curtis 2009; Snieder & Fleury 2010; Fleury *et al.* 2010). By conducting the same experiment in Fig. 6, but for the case of full passive-source illumination, the artefacts in the cross-correlation results (Fig. 7c) are significantly reduced. This is an expected result under full-angle illumination conditions in a scattering medium (van Tiggelen 2003; Margerin & Sato 2011). Nonetheless, artefacts still considerably obscure the target primary reflections when compared to the associated reference response (Fig. 6b). This is likely due to the complex mixture of *P* and *S* waves that make up the modelled passive-source wavefields, which we generate by implementing double-couple sources with random orientation and amplitude. Moreover, the passive sources that illuminate the array directly from below are implemented right above the target Moho reflector, which is known to be a source of artefacts for the cross-correlation method (Snieder 2006). These factors inevitably cause irregular passive-source illumination that cross-correlation cannot correct for without dedicated further processing (Curtis & Halliday 2010; Almagro Vidal *et al.* 2014). The ballistic MDD results show that the inherent illumination-balancing effect of this method results in a relative improvement with respect to the cross-correlation results by slightly decreasing the visibility of artefacts (Fig. 6e). This is due to its ballistic PSF, which is designed to compensate for irregularities in the passive-source wavefield (Wapenaar *et al.* 2008).

The full-field MDD proves to be more effective than the other SI methods in estimating the primary reflections in case of a strongly scattering overburden under more optimal illumination conditions: the primary-reflection estimates correspond well to the reference response in terms of TWT and AVO (Fig. 7d). This indicates that multiple scattering gives rise to other effects that are compensated for by full-field MDD but not by cross-correlation nor ballistic MDD. The fact that the radiation pattern of a scatterer is similar to that of a source plays a significant role in increasing the complexity of the scattered wavefield (Fig. 8a). In fact, secondary illumination provided by the multiple scattering in the overburden can exhibit an irregular illumination pattern (Fig. 8b). The full-field PSF has the advantage that it encodes the complex wavefield phenomena

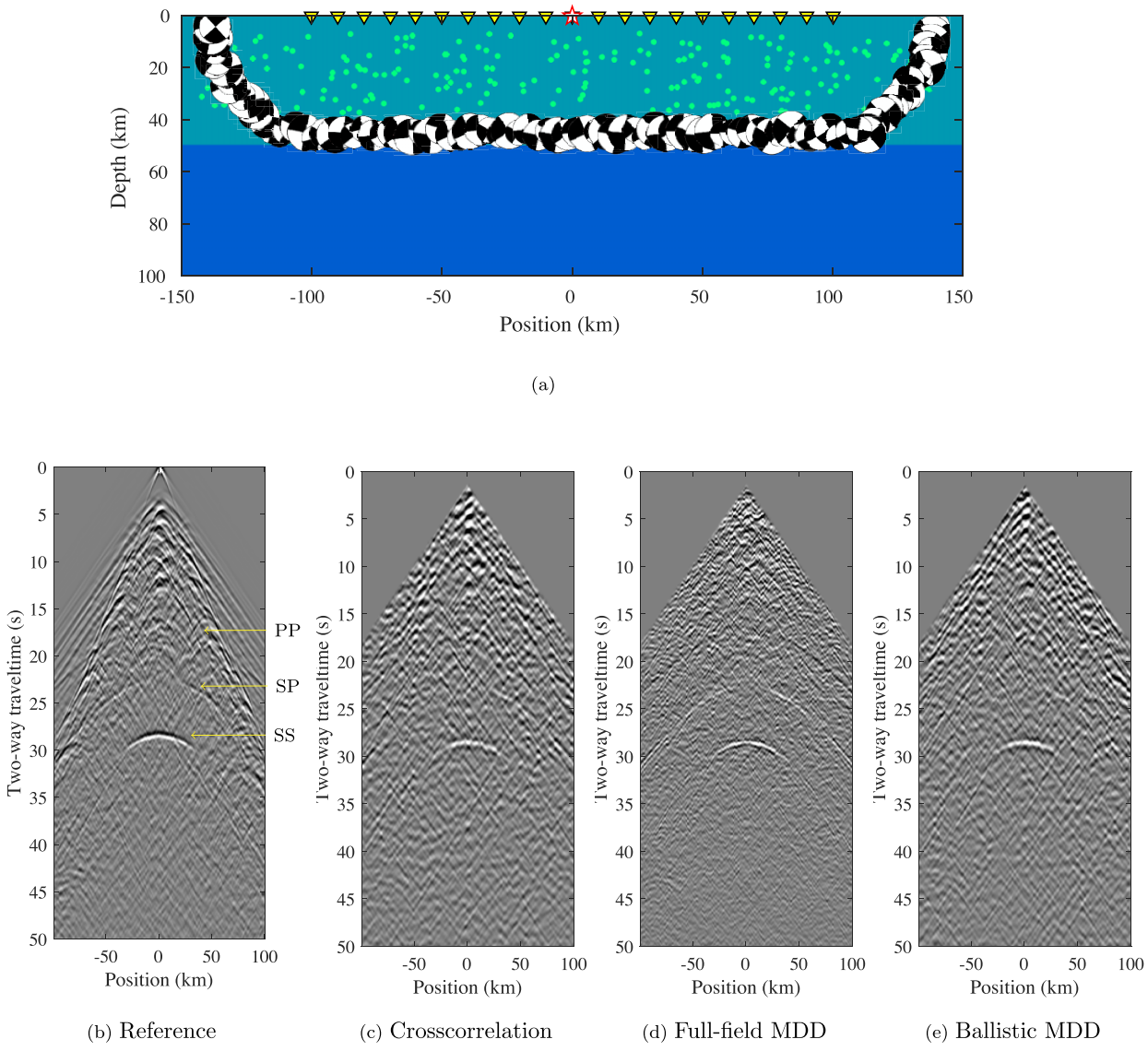

Figure 7. As Fig. 2, but with 200 scatterers in the crust and full illumination.

that are characteristic of scattering-induced illumination. Since irregular illumination is not corrected for by the cross-correlation method, it causes distortions of the virtual-source radiation pattern. The ballistic MDD method cannot compensate for irregularities in the scattered wavefields either, because it only balances out direct wavefield illumination.

3.2 Scattering strength as a diagnostic measure for SI

Our results show that in case of limited illumination conditions, there exists a trade-off between the completeness of the reconstructed virtual primary reflections and the scattering strength of the crust. This indicates that it may be possible to use a measure of the scattering strength to determine whether it is appropriate to apply SI methods in a certain area for a given frequency range. It is important to point out that this trade-off is not the same for all SI methods. For example, for the lithospheric model we analyse here: in the 50-scatterer model (Fig. 5a), all SI methods can be applied. While in the case of the model with 200 scatterers (Fig. 6a), our results indicate that only full-field MDD is suitable to estimate virtual primary reflections. This indicates that a determination of the scattering strength in a given area can help to determine the reliability of SI methods.

3.3 Avenues for future research

In this study, we found that the performance of SI methods relies on the scattering strength of the crust. However, in practice the scattering strength of the crust is not known and would need to be estimated *a priori*. An effective method that can be used to determine the scattering strength of the crustal lithosphere is, for example, the inversion-based method `QOpen` (Eulenfeld & Wegler 2016). This open-source tool is an improved form of the multi-lapse time window analysis from Hoshiba *et al.* (1991) and Fehler *et al.* (1992). It uses the energy partitioning between ballistic and coda wavefield to separate intrinsic from scattering attenuation and therefore offers a reliable estimate of the scattering strength of the heterogeneous crust.

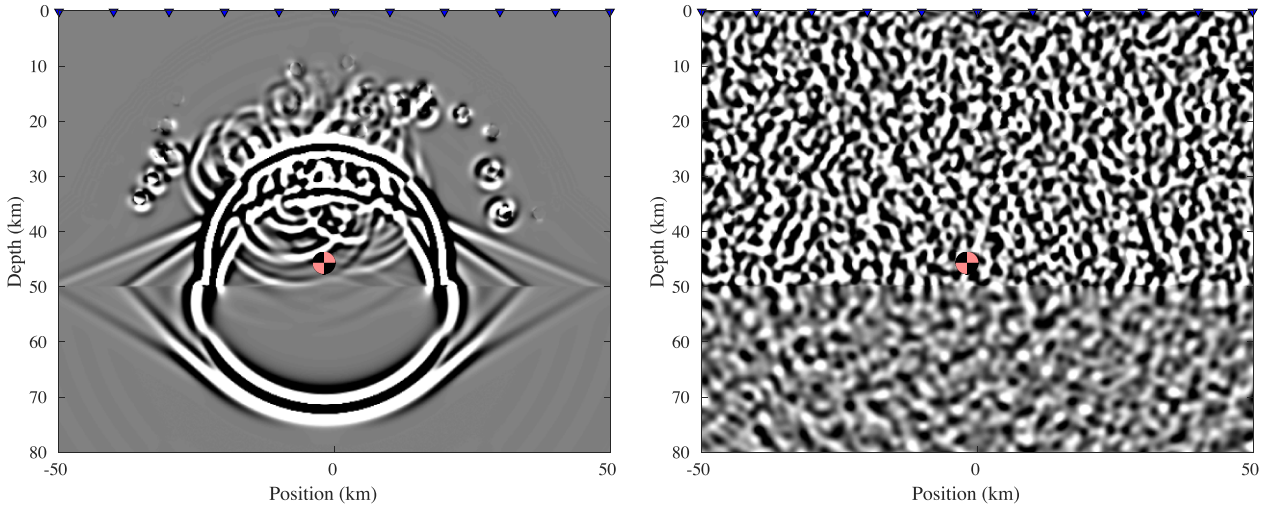

Figure 8. Numerical lapse time development of *S*-potential scattering coda generated by a double-couple source positioned at coordinates (−2, 46) in the model with 200 scatterers (Fig. 7a). (a) Snapshot after 6 s: note that the propagating *P* wavefield is detected when it interacts with the scatterers, thus yielding *P–SV* scattering radiation patterns. (b) In this snapshot after 95 s, the complex nature of the scattered wavefield reaching the acquisition surface can be observed.

Furthermore, this study revealed several valuable properties of full-field MDD that could pave the way for novel scientific applications. First of all, we found that the primaries estimated by full-field MDD are hardly polluted by surface waves. This is because full-field MDD estimates the Green's function response of the equivalent medium without free surface, which obviates the need to remove surface waves by *fk*-filtering prior to body-wave processing. We also discovered that full-field MDD succeeded in estimating several virtual diffraction hyperbolae of crustal scatterers. This creates possibilities for the application of diffraction imaging routines to use virtual shot gathers for high-resolution imaging of heterogeneities in the subsurface (Khaidukov *et al.* 2004). Our findings show that full-field MDD exploits the full spectral bandwidth of the entire scattered wavefield (Fig. 4), which effectively increases the resolution of the resulting virtual shot gather without requiring further processing. This indicates that a higher resolution diffraction image of the scatterers could be achieved from virtual responses obtained by full-field MDD than, for example, would be possible with the virtual responses estimated by cross-correlation.

4 CONCLUSION

This numerical study shows that there exists a trade-off between the scattering strength in an area and the ability of body-wave interferometry methods to reconstruct virtual primary reflections under limited illumination conditions. The results demonstrate that while multiple scattering helps to fill illumination gaps, it is also associated with a higher abundance of artefacts that can severely obscure virtual primary reflections reconstructed by SI. However, not all SI methods evaluated in this study are equally affected by artefacts. For the models that contain a heterogeneous crustal overburden, cross-correlation and ballistic MDD are strongly affected by artefacts in both limited and full illumination conditions. Under the same conditions, the full-field MDD method estimates virtual *P*- and *S*-wave primary reflections that are considerably less affected. Moreover, we find that the performance of the SI methods depends on the scattering strength: the presence of 50 crustal scatterers had beneficial effects for all methods, while only the full-field MDD method still yielded acceptable results for the model with the highest scattering strength. These findings indicate that it is recommendable to use full-field MDD over other SI methods for body-wave reflection estimation in real-data scenarios characterized by multiple scattering. Finally, we see potential to use an estimate of the scattering strength as a diagnostic measure to determine whether primary estimation by a given SI method is reliable in a specific site. To reach this point of maturity of the approach, a systematic analysis of SI methods is required for more scenarios that include intrinsic absorption and cover a broader range of scattering strengths, illumination conditions and frequencies.

ACKNOWLEDGMENTS

We express our gratitude to two anonymous reviewers for their significant contribution to improving the quality of this manuscript.

DATA AVAILABILITY

The numerical experiments in this study are conducted using the elastic module of the open-source finite-difference modelling software `fdelmodc`, which can be downloaded by following this link: fdelmodc-source-code. All processing steps are implemented using the MATLAB programming language. The synthetic data set underlying this paper will be shared on reasonable request to the authors.

REFERENCES

Aki, K., 1969. Analysis of the seismic coda of local earthquakes as scattered waves, *J. geophys. Res.,* **74**(2), 615–631.

Aki, K., 1992. Scattering conversions P to S versus S to P, *Bull. seism. Soc. Am.,* **82**(4), 1969–1972.

Almagro Vidal, C., 2017. *Passive seismic interferometry for reflection imaging and monitoring,* Ph.D. thesis, Delft University of Technology.

Almagro Vidal, C., Draganov, D., van der Neut, J., Drijkoningen, G. & Wapenaar, K., 2014. Retrieval of reflections from ambient noise using illumination diagnosis, *Geophys. J. Int.,* **198**(3), 1572–1584.

Almagro Vidal, C., van der Neut, J., Verdel, A., Hartstra, I.E. & Wapenaar, K., 2018. Passive body-wave interferometric imaging with directionally constrained migration, *Geophys. J. Int.,* **215**(2), 1022–1036.

Boiero, D., Mahat, S., Bagaini, C. & Ortin, M., 2023. True-amplitude multiple prediction in sparse ocean-bottom acquisitions using a multidimensional deconvolution approach, in *84th EAGE Annual Conference and Exhibition,* Vol. **2023**(1), pp. 1–5.

Campillo, M., 2006. Phase and correlation in random seismic fields and the reconstruction of the green function, *Pure appl. Geophys.,* **163,** 475–502.

Campillo, M. & Paul, A., 2003. Long-range correlations in the diffuse seismic coda, *Science,* **299**(5606), 547–549.

Chamarczuk, M., Malinowski, M. & Draganov, D., 2021. 2D body-wave seismic interferometry as a tool for reconnaissance studies and optimization of passive reflection seismic surveys in hardrock environments, *J. appl. Geophys.,* **187,** 104288.

Curtis, A. & Halliday, D., 2010. Directional balancing for seismic and general wavefield interferometry, *Geophysics,* **75**(1), SA1–SA14.

Derode, A., Larose, E., Tanter, M., De Rosny, J., Tourin, A., Campillo, M. & Fink, M., 2003. Recovering the Green's function from field-field correlations in an open scattering medium (L), *J. acoust. Soc. Am.,* **113**(6), 2973–2976.

Dziewonski, A.M. & Anderson, D.L., 1981. Preliminary reference earth model, *Phys. Earth planet. Inter.,* **25**(4), 297–356.

Eulenfeld, T. & Wegler, U., 2016. Measurement of intrinsic and scattering attenuation of shear waves in two sedimentary basins and comparison to crystalline sites in germany, *Geophys. J. Int.,* **205**(2), 744–757.

Fehler, M., Hoshiba, M., Sato, H. & Obara, K., 1992. Separation of scattering and intrinsic attenuation for the Kanto-Tokai region, Japan, using measurements of S-wave energy versus hypocentral distance, *Geophys. J. Int.,* **108**(3), 787–800.

Fleury, C., Snieder, R. & Larner, K., 2010. General representation theorem for perturbed media and application to Green's function retrieval for scattering problems, *Geophys. J. Int.,* **183**(3), 1648–1662.

Halliday, D. & Curtis, A., 2009. Seismic interferometry of scattered surface waves in attenuative media, *Geophys. J. Int.,* **178**(1), 419–446.

Hartstra, I.E., Almagro Vidal, C. & Wapenaar, K., 2017. Full-field multidimensional deconvolution to retrieve body-wave reflections from sparse passive sources, *Geophys. J. Int.,* **210**(2), 609–620.

Hartstra, I.E., Almagro Vidal, C. & Wapenaar, K., 2018. Retrieval of elastodynamic reflections from passive double-couple recordings, *J. geophys. Res.: Solid Earth,* **123**(4), 3197–3207.

Heller, G., Margerin, L., Sébe, O., Mayor, J. & Calvet, M., 2022. Revisiting multiple-scattering principles in a crustal waveguide: equipartition, depolarization and coda normalization, *Pure appl. Geophys.,* **179,** 1–35.

Hoshiba, M., Sato, H. & Fehler, M., 1991. Numerical basis of the separation of scattering and intrinsic absorption from full seismogram envelope, *Papers Meteorol. Geophys.,* **42**(2), 65–91.

Khaidukov, V., Landa, E. & Moser, T., 2004. Diffraction imaging by focusing-defocusing: an outlook on seismic superresolution, *Geophysics,* **69,** 1478–1490.

Larose, E., Derode, A., Campillo, M. & Fink, M., 2004. Imaging from one-bit correlations of wideband diffuse wave fields, *J. appl. Phys.,* **95**(12), 8393–8399.

Larose, E., Roux, P., Campillo, M. & Derode, A., 2008. Fluctuations of correlations and Green's function reconstruction: role of scattering, *J. appl. Phys.,* **103,** 1–11.

Malcolm, A.E., Scales, J.A. & van Tiggelen, B.A., 2004. Extracting the Green function from diffuse, equipartitioned waves, *Phys. Rev. E,* **70,** 015601(R).

Margerin, L. & Sato, H., 2011. Reconstruction of multiply-scattered arrivals from the cross-correlation of waves excited by random noise sources in a heterogeneous dissipative medium, *Wave Motion,* **48**(2), 146–160.

Margerin, L., Campillo, M. & Tiggelen, B., 1998. Radiative transfer and diffusion of waves in a layered medium: new insight into coda Q, *Geophys. J. Int.,* **134**(2), 596–612.

Margerin, L., Campillo, M., Shapiro, N.M. & van Tiggelen, B., 1999. Residence time of diffuse waves in the crust as a physical interpretation of coda Q: application to seismograms recorded in Mexico, *Geophys. J. Int.,* **138**(2), 343–352.

Mohorovičić, A., 1910. Rgodisnje izvjesce zagrebackog meteoroloskog opservatorija za godinu., *Jahrb. Meteorol. Obs. Zagreb,* **9**(4), 1–63.

Mooney, W. & Meissner, R., 1992. Multi-genetic origin of crustal reflectivity: a review of seismic reflection profiling of the continental lower crust and Moho, in *Continental Lower Crust,* pp. 45–79, Elsevier Amsterdam.

Nakata, N., Snieder, R. & Behm, M., 2014. Body-wave interferometry using regional earthquakes with multidimensional deconvolution after wavefield decomposition at free surface, *Geophys. J. Int.,* **199**(2), 1125–1137.

Paasschens, J. C.J., 1997. Solution of the time-dependent Boltzmann equation, *Phys. Rev. E,* **56**(1), 1135–1140.

Roux, P., Sabra, K.G., Gerstoft, P. & Kuperman, W.A., 2005. P-waves from cross-correlation of seismic noise, *Geophys. Res. Lett.,* **32**(L19303), 2–4.

Ruigrok, E., Campman, X. & Wapenaar, K., 2011. Extraction of p-wave reflections from microseisms, *C. R. Geosci.,* **343,** 512–525.

Sato, H., Fehler, M.C. & Maeda, T., 2012. *Seismic Wave Propagation and Scattering in the Heterogeneous Earth,* Springer, 2nd edn.

Snieder, R., 2002. Coda wave interferometry and the equilibration of energy in elastic media, *Phys. Rev. E,* **66**(4), 046615.

Snieder, R., 2004. Extracting the Green's function from the correlation of coda waves: a derivation based on stationary phase, *Phys. Rev. E,* **69**(4), 046610.

Snieder, R., 2006. Spurious multiples in seismic interferometry of primaries, *Geophysics,* **71**(4), SI111–SI124.

Snieder, R. & Fleury, C., 2010. Cancellation of spurious arrivals in Green's function retrieval of multiple scattered waves, *J. acoust. Soc. Am.,* **128**(4), 1598–1605.

Stein, S. & Wysession, M., 2003. *An Introduction to Seismology, Earthquakes, and Earth Structure,* Blackwell Publishing.

Thorbecke, J.W. & Draganov, D., 2011. Finite-difference modeling experiments for seismic interferometry, *Geophysics,* **76,** H1–H18.

van der Neut, J. & Herrmann, F.J., 2013. Interferometric redatuming by sparse inversion, *Geophys. J. Int.,* **192,** 666–670.

van Tiggelen, B., 2003. Green function retrieval and time reversal in a disordered world, *Phys. Rev. Lett.,* **91**(24), 243904.

Wang, W. & Shearer, P.M., 2019. An improved method to determine Coda-Q, earthquake magnitude, and site amplification: theory and application to Southern California, *J. geophys. Res.: Solid Earth,* **124**(1), 578–598.

Wapenaar, K. & Fokkema, J., 2006. Green's function representations for seismic interferometry, *Geophysics,* **71,** SI33–SI46.

Wapenaar, K., van der Neut, J. & Ruigrok, E., 2008. Passive seismic interferometry by multidimensional deconvolution, *Geophysics,* **73**(6), A51–A56.

Weaver, R.L., 1982. On diffuse waves in solid media, *J. acoust. Soc. Am.,* **71**(6), 1608–1609.

Wu, R.-S. & Aki, K., 1985. Scattering characteristics of elastic waves by an elastic heterogeneity, *Geophysics,* **50**(4), 582–595.